PERGAMON

International Journal of Heat and Mass Transfer 41 (1998) 3537–3550

International Journal of HEAT and MASS TRANSFER

Isolated fluid oxygen drop behavior in fluid hydrogen at rocket chamber pressures

K. Harstad, J. Bellan*

Jet Propulsion Laboratory, California Institute of Technology, Pasadena, CA 91109, U.S.A.

Received 7 May 1997; in final form 5 January 1998

Abstract

A model has been developed for the behavior of an isolated fluid drop of a single compound immersed into another compound in finite, quiescent surroundings at supercritical conditions. The model is based upon fluctuation theory which accounts for both Soret and Dufour effects in the calculation of the transport matrix relating molar and heat fluxes to the transport properties and the thermodynamic variables. The transport properties have been modeled over a wide range of pressure and temperature variation applicable to LO_x–H_2 conditions in rocket chambers, and the form of the chemical potentials is valid for a general fluid. The equations of state have been calculated using a previously-derived, computationally-efficient and accurate protocol. Results obtained for the LO_x–H_2 system show that the supercritical behavior is essentially one of diffusion. The temperature profile relaxes fastest followed by the density and lastly by the mass fraction profile. An effective Lewis number calculated using theory derived elsewhere shows that it is larger by approximately a factor of 40 than the traditional Lewis number. The parametric variations show that gradients increasingly persist with increasing fluid drop size or pressure, and with decreasing temperature. The implication of these results upon accurate measurements of fluid drop size under supercritical conditions is discussed. © 1998 Elsevier Science Ltd. All rights reserved.

Nomenclature

A_d fluid drop surface area
C_p molar heat capacity at constant pressure
D diffusion coefficients
F_{ems} emission flux
h molar enthalpy
h_p Planck's constant
J molar flux
$\mathbf{L}$ transport matrix
L_{ij} elements of the transport matrix $\mathbf{L}$
Le Lewis number
m molar mass
M fluid drop mass
Ma Mach number
n number of moles per unit volume
N number of species
p pressure
q heat flux
r radial coordinate
R_d drop radius
R_u universal gas constant
t time
T temperature
u velocity
u_T mean, normal velocity of a molecule due to thermal fluctuations
v molar volume
x generic coordinate
X mole fraction
Y mass fraction
Z compressibility factor.

Greek symbols

α_a accommodation coefficients
α_D mass diffusion factors
α_T thermal diffusion factor
α_v thermal expansion ratio
β $1/(R_uT)$
γ activity coefficient

* Corresponding author. Tel.: 001 818 354 6959; fax: 001 818 393 5011; e-mail: Josette.Bellan@jpl.nasa.gov

0017–9310/98 $19.00 © 1998 Elsevier Science Ltd. All rights reserved
PII: S0017–9310(98)00049–0

Δh latent heat
η viscosity
κ_s isentropic compressibility
κ_T isothermal compressibility
λ thermal conductivity
μ chemical potential
v_ρ dissipative expansion
ρ density
τ stress tensor
Φ_v viscous dissipation
φ gas fugacity coefficient.

Subscripts
α, β coordinate notation
b drop interface, at $r = R_d$
c critical point property
d drop
eff effective
equil thermodynamic equilibrium
evap evaporation
g grid
i, j species
m mass
r radial component
sat saturation
si at the edge of the sphere of influence
T thermal
∞ far field.

Superscripts
G on the initial hydrogen side
i, j species
liq liquid
L on the initial oxygen side
0 initial value
$''$ pure substance.

1. Introduction

Liquid rocket engine design is not a mature technology in that the issues of reliability and efficiency are unresolved. Current designs are still based upon empirical knowledge and theory that does not portray the complexities of the physical processes and of the environment in the combustion chambers. The extensive review on liquid propellant rocket instabilities compiled by Harrje and Reardon [1] more than twenty years ago remains the base of rocket design despite the increased understanding that many of the approximations made in performing the calculations compromise the validity of the results.

One of the foundations of liquid rocket instabilities is the theory of isolated drop evaporation and combustion in an infinite medium [1, 2]. The early version of that theory was based on the assumption of quasi-steady gas behavior with respect to the liquid phase, an assumption strictly valid only at low pressures where the liquid density is three orders of magnitude larger than that of the gas. Recognizing that at the elevated pressures of liquid rocket chambers the liquid density approaches that of the gas, the quasi-steady assumption was relaxed in other investigations [3–7]. However, it is only recently that the description of the full complexity of combustion chambers processes was undertaken; this includes not only the complete unsteady treatment of the conservation equations but also appropriate equations of state with consistent mixing rules and transport properties valid over transcritical/supercritical conditions.

The discussion below emphasizes the LO_x system because its behavior sometimes contrasts with that observed for hydrocarbons as noted by Chesnau et al. [8]. Therefore, the results of many interesting studies in the context of Diesel engines or high-pressure gas turbine engines will not be discussed. Such a discussion appears in the review of Givler and Abraham [9].

Yang et al. [10] described the vaporization of a liquid oxygen drop (LO_x) in hydrogen over a wide range of pressures. The model includes thermodynamic non-idealities, variable properties and the assumption of liquid–vapor equilibria. The Soret term accounting for species transport due to thermal gradients and the Dufour term accounting for heat transfer resulting from concentration gradients are neglected. In the side of the drop boundary containing hydrogen, the Soave–Redlich–Kwong (SRK) equation of state (EOS) is used to calculate the compressibility factor while the density of fluid in the LO_x side of the boundary is given by curve-fitted experimental data. The thermal conductivities and heat capacities are correlated as functions of density and temperature, the liquid diffusivity is estimated following Scheibel's [11] procedure, and the binary diffusion coefficients are calculated following the corresponding states method of Takahashi [12]. Calculations are initiated with a drop at subcritical temperature in surroundings where the pressure and temperature are both above the critical point; once the drop surface temperature reaches the critical point, the assumption is made that it is this surface that continues to define a gas/liquid interfacial boundary and thus, it is its motion that defines the drop regression rate. This surface tracks thus the progression of a liquid entity composed of both LO_x and hydrogen in contrast to the pure LO_x drop. Plots of the temperature, mole fraction and density all show steep gradients around what is presumably the interface (the interfacial boundary is not indicated on the curves). Because the radial coordinate is logarithmic, it is impossible to compare the detailed evolution of the heat vs. the mass transfer; however, plots of the Lewis number show that it reaches values as large as 1.9 on the hydrogen side and 1.3 in the LO_x side. The results show the increasing importance of hydrogen diffusion into LO_x and the increase in vaporization rate with increasing

pressure. Surprisingly, the results show that the classical, quasi-steady-derived D^2-law [2] remains valid for all pressures (5–250 atm) and drop diameters (5×10^{-6}–300×10^{-6} m). Hsiao et al. [13] extended the study of [10] to include convective effects. In this new version, the Benedict–Webb–Rubin (BWR) EOS in conjunction with an extended corresponding states principle, replaces the SRK EOS for the purpose of achieving higher-accuracy density predictions and the corresponding states principle is applied to calculate transport properties. Results from the calculation show that the interface defined by the critical temperature deforms and stretches throughout the drop lifetime presenting a convex surface to the incoming flow. The motion of the drop is defined by the motion of its center of gravity and a drag coefficient is calculated.

The model of Delplanaque and Sirignano [14] is similar to that of [10] in that Soret and Dufour effects are neglected and phase equilibrium is assumed; additionally, since the calculations are not pursued beyond the drop surface reaching the critical point, the mixture is approximated by a gas with mixture-averaged properties. The Chueh and Prausnitz [15] version of the Redlich–Kwong (RK) EOS is used and the thermophysical and transport properties are correlated from data with no correction for real gas behavior. The diffusion coefficients are calculated using dilute gas theory and it is uncertain whether the discussed high-pressure effects [16] are included. The liquid density is evaluated using the Hankinson–Brobst–Thomson method [16] and the isobaric heat capacity is obtained through an ideal gas correlation [16]. Since there is a unique relationship between heat capacities and the enthalpy as expressed by the EOS, it is not clear that this thermodynamic relationship is satisfied by this procedure. Results from the calculations show that the LO_x drop surface reaches the critical temperature in a time much smaller than the characteristic thermal diffusion time.

More recently, Haldenwang et al. [17] constructed a model similar to those in [10] and [14], but identified the drop surface with the location where thermodynamic equilibrium occurs. The RKS EOS is used in the model and C_p is estimated independently of the EOS, possibly introducing inconsistencies in the thermodynamics. The binary diffusion coefficients were calculated through empirical correlations [16] in liquids and dense gas, and the thermal conductivity was calculated using standard mixing rules and experimental data for pure substances. In this study, the subcritical regime is defined as that for which the mass fraction at the surface remains higher than that corresponding to the value for which the surface temperature is the critical temperature during the entire drop lifetime. With this definition, the evolution of a LO_x drop initially at 100 K in surroundings at 1000 K and 8 MPa is classified as subcritical behavior although obviously there is no material drop surface at those conditions. Calculations performed with different thermodynamic properties yield results qualitatively similar but quantitatively different. Just as in [10], the D^2-law remains valid both in the subcritical and supercritical regimes. Comparisons with the microgravity observations of Sato [18] for *n*-octane show similar trends: the drop lifetime decreases with increasing pressure in the subcritical regime and increases with increasing pressure in the supercritical regime. To evaluate the impact of the assumed interface location (at the critical temperature [10] vs. the saturation temperature [17]), results are presented with the model of [17] using each assumption, and they are further compared with those of [10]; although there is qualitative agreement between the drop lifetime vs. the reduced pressure curves found by the authors using each assumption, their variation is not similar to that of [10]. A further detailed evaluation of the influence of the interface definition reveals that, in contrast to the situation when the interface is located at the critical point, an increase in radius is obtained in the transcritical regime when the surface is assumed to be at thermodynamic equilibrium. This effect is attributed to the increase in the difference between equilibrium mass fraction and critical mass fraction with increasing pressure. The obvious conclusion from this study is that it is not only the conservation equations, EOS, and transport properties that must be accurately modeled, but also the interface processes.

Haldenwang et al. [17] also note that the results of [10] and [14] for identical conditions have more than one order of magnitude discrepancy, and that their own results do not agree with those of either one of these studies; this indicates that it is only through comparisons with experiments that the cause of the difference could be resolved. However, experiments with LO_x–hydrogen combinations are prohibitively expensive because of the associated safety aspect. Additionally, the interpretation of the results is not straightforward as will be discussed below.

Circumventing the difficulty of LO_x in hydrogen and that of very high pressures, Chesnau et al. [8] present a set of experiments for LO_x evaporation in air, nitrogen and helium at 0.1 MPa and 3 MPa. Since the data was acquired through imaging, the drop surface is a measure of steep density gradients. The data shows that at 0.1 MPa, the D^2-law is validated within the range of experimental error. In contrast, at 2 MPa the slope of D^2 changes with time, which is documented as an unsteadiness in the evaporation constant; this unsteadiness increases with increasing pressure. These observations seem to disprove the previous theoretical predictions of the D^2-law holding over the entire subcritical range. More recently, Chauveau and Gökalp [19] acquired data for LO_x in helium at up to 65 bars under gravity conditions. The drop was suspended from a fiber, indicating that it was not pure LO_x which becomes supercritical (and thus,

has zero surface tension) at 5.043 MPa. Both sets of data show that the evaporation rate increases with increasing pressure, unlike the data of Sato et al. [18] for *n*-octane and that of Chauveau et al. [20, 21] for *n*-heptane and methanol showing a minimum in the evaporation rate at the critical point. Chesnau et al. [8] attempt to explain the difference between the variation of the evaporation rate of LO_x and hydrocarbons with pressure on the basis of the reduced temperature in the drops surroundings which in their experiments was supercritical for LO_x but subcritical for the hydrocarbons. This explanation is not convincing since the data of Sato et al. [18] was acquired for burning *n*-octane drops and therefore at supercritical surrounding temperature since the critical temperature of *n*-octane is 570 K. Therefore, the qualitative agreement between Haldenwang et al.'s drop lifetime variation with pressure for LO_x [17] and the observations of Sato et al. [18] is suspicious and may indicate a flaw in the model rather than a validation of the model.

The above discussion shows that there is still a wide gap between the current modeling capability of LO_x drops in hydrogen and that necessary for advancing the state of the art in liquid rocket motor design. The model presented below constitutes an improvement over the existing models in that it includes Soret and Dufour effects, an accurate form of the chemical potentials valid for general fluids, and thermodynamic nonequilibrium between phases, none of which were included in [17, 10, 13, 14]. This set of conservation equations and a kinetic law (equivalent to the Langmuir–Knudsen law that is valid for liquid evaporation) derived here for dense gas are coupled with accurate EOSs and transport coefficients over the subcritical/supercritical range for both LO_x and hydrogen. The model used for the EOSs has been described in detail elsewhere [22]; these EOSs are obtained by curve fitting data and further extrapolation using the concept of departure function [16]. The importance of Soret and Dufour effects is the subject of discussions in Harstad and Bellan [23] while the thermodynamic equilibrium assumption is shown by Bellan and Summerfield [24] to be unrealistic in certain situations even under subcritical conditions.

2. Model

The model of the conservation equations is based on the fluctuation theory of Keizer [25], also described by Peacock-Lopez and Woodhouse [26]. The advantage of this theory is that it inherently accounts for nonequilibrium processes and naturally leads to the most general fluid equations by relating the partial molar fluxes, $\mathbf{J}_i$, and the heat flux, $\mathbf{q}$, to thermodynamic quantities.

2.1. Conservation equations

In general form, the conservation equations are:

—continuity

$$\frac{\partial \rho}{\partial t}+\frac{\partial(\rho u_\beta)}{\partial x_\beta}=0 \tag{2.1}$$

where the conventional index notation for expressing derivatives and sums apply.

—momentum conservation on the α direction

$$\frac{\partial(\rho u_\alpha)}{\partial t}+\frac{\partial(\rho u_\alpha u_\beta)}{\partial x_\beta}+\frac{\partial p}{\partial x_\alpha}=\frac{\partial \tau_{\alpha\beta}}{\partial x_\beta} \tag{2.2}$$

where $\tau_{\alpha\beta}=\eta_{\mathrm{mix}}[(\partial u_\alpha/\partial x_\beta+\partial u_\beta/\partial x_\alpha)-(2/3)\delta_{\alpha\beta}\,\partial u_\gamma/\partial x_\gamma]$ is the stress tensor in which $\delta_{\alpha\beta}$ is a tensor having unit diagonal, its other components being null.

—species conservation

$$\frac{\partial \rho_i}{\partial t}+\frac{\partial(\rho_i u_\beta+m_i J_{i\beta})}{\partial x_\beta}=0 \tag{2.3}$$

—enthalpy equation

$$\frac{\partial(nh)}{\partial t}+\frac{\partial(nhu_\beta)}{\partial x_\beta}=\frac{\partial p}{\partial t}+u_\beta\frac{\partial p}{\partial x_\beta}-\frac{\partial q_\beta}{\partial x_\beta}+\Phi_v \tag{2.4}$$

where $\Phi_{\mathrm{v}}=\tau_{\alpha\beta}\,\partial u_\alpha/\partial x_\beta$ is the viscous dissipation and $n=\rho/m$.

Fluctuation theory relates $\mathbf{J}_i$ and $\mathbf{q}$ to the transport matrix $\mathbf{L}$ through

$$\mathbf{J}_i=L_{iq}\nabla\beta-\sum_j^N L_{ij}\nabla(\beta\mu_j),\quad \mathbf{q}=L_{qq}\nabla\beta-\sum_j^N L_{qj}\nabla(\beta\mu_j). \tag{2.5}$$

Here L_{ij} are the Fick's diffusion elements, L_{qq} is the Fourier thermal diffusion element, L_{iq} are the Soret diffusion and L_{qj} are the Dufour diffusion elements and $\beta\equiv 1/(R_{\mathrm{u}}T)$. The Onsager relations state that $L_{ij}=L_{ji}$ and $L_{iq}=L_{qi}$. Additionally, conservation of fluxes and mass in the system imply that $\Sigma_i^N m_i\mathbf{J}_i=\mathbf{0}$ and $\Sigma_i^N L_{ij}m_i=0$ for $j\in[1,N]$ and $j=q$.

Using the thermodynamic relationship

$$\mathrm{d}(\beta\mu_j)=\beta(v_j\,\mathrm{d}p-h_j\,\mathrm{d}\ln T)+\left(\sum_1^{N-1}\alpha_{\mathrm{D}ji}\,\mathrm{d}X_i\right)\Big/X_j \tag{2.6}$$

where

$$\alpha_{\mathrm{D}ij}\equiv\beta X_i\partial\mu_i/\partial X_j=\partial X_i/\partial X_j+X_i\,\partial\ln\gamma_i/\partial X_j \tag{2.7}$$

one can calculate $\mathbf{J}_i$ from (2.5) and (2.6).

In general, this formalism proceeds with the definition of a symmetric matrix whose elements are the pair-wise mass diffusion coefficients for the mixture $D_{\mathrm{mix}}^{(ij)}$, and an antisymmetric matrix whose elements are the thermal diffusion factors $\alpha_{\mathrm{T}}^{(ij)}$. For a binary mixture, this formalism simplifies considerably to yield

$$\mathbf{J}_1=-(m_2/m)(\mathbf{J}_\alpha+X_1X_2\alpha_{\mathrm{T}}nD_{\mathrm{m}}\nabla\ln T). \tag{2.8}$$

$D_{\mathrm{m}}=L_{11}(m/m_2)^2v/(X_1X_2)$ is a mass diffusion coefficient,

$\alpha_T = (L_{1q}/L_{11})\beta m_2/m$ is the ratio between the thermal and mass diffusivities, and

$$\mathbf{J}_\alpha = nD_m\{\alpha_D\nabla X_1 + \beta[m_1m_2X_1X_2/m][(v_1/m_1 - v_2/m_2)\nabla p + (h_2/m_2 - h_1/m_1)\nabla \ln T]\}. \quad (2.9)$$

According to equation (2.7) $\alpha_D = 1 + X_1(\partial \ln \gamma_1/\partial X_1)_{T,p}$, where from the Gibbs–Duhem relationship $\alpha_{D11} = \alpha_{D22} = -\alpha_{D12} = -\alpha_{D21} = \alpha_D$. Further, equation (2.3) can be simplified to yield

$$\frac{DX_1}{Dt} = -\frac{m}{m_2 n}\nabla\cdot\mathbf{J}_1 = -\frac{DX_2}{Dt} \quad (2.10)$$

where $DX_1/Dt \equiv \partial X_1/\partial t + u_\beta \partial X_1/\partial x_\beta$, and $X_1 = m_2Y_1/[m_1 + (m_2 - m_1)Y_1]$. Combining equations (2.4), (2.8) and (2.9) one obtains

$$nC_p\frac{DT}{Dt} = \alpha_v T\frac{Dp}{Dt} - \nabla\cdot\mathbf{q} + \Phi_v + m_1(h_1/m_1 - h_2/m_2)\nabla\cdot\mathbf{J}_1 \quad (2.11)$$

where $\alpha_v = [(\partial v/\partial T)_{p,X_1}]/v$ and

$$\mathbf{q} = -(\alpha_T R_u T)\mathbf{J}_\alpha - \lambda\nabla T. \quad (2.12)$$

Consistent with the previous definitions, $\lambda = \beta L_{qq}/T$.

2.2. Boundary conditions

For the spherical drops considered here, boundary conditions must be applied at three different locations: the fluid drop center, the interface which is initially between the pure LO_x drop and the fluid, and the far field. In this model, the far field is set at a finite location, which is a multiple of the initial fluid drop radius, from the initial interface. Consistent with previous terminology from subcritical theory [27], this far field location is called the edge of the 'sphere of influence' and is located at R_{si}.

At the center of each entity, spherical symmetry conditions prevail, whereas at the edge of the sphere of influence known conditions apply.

The conditions at the interface express not only conservation of mass, species, momentum and energy, but also nonequilibrium evaporation and solvation. Initially, LO_x exists for $r < R_d$ and the superscript L is used in this side of the interface. At $t = 0$, a fluid that is primarily H_2 surrounds the drop and the superscript G is used for $r > R_d$. In contrast to the purely subcritical situation [27] where the interface is well defined by a surface where there is a sharp change in density, here there is an arbitrariness in defining an interface that should be followed in time. As we show in the Results section, the gradients of the mass fraction and density do not coincide, so that following the pure drop interface is not equivalent to following the maximum density gradient which is what is optically detected. Since at supercritical conditions the physical phase change interface does not exist, we are free to choose an interface that we want to follow. Ultimately, under subcritical conditions the choice has to be consistent with the purely subcritical theory.

Since previous results have shown that nonequilibrium effects can be important [24], we do not make the assumption of equilibrium evaporation utilized by all other investigators (cf. [17, 10, 14]). The equilibrium evaporation essentially specifies the mass fraction in the gas side once the mass fraction in the drop side and the temperature at the surface are known. The small characteristic time of thermodynamic equilibration introduces another complication in the boundary conditions because it renders the equations very stiff. Nevertheless, nonequilibrium must be considered since there is no physical justification for equilibrium.

Simple accounting of unknowns at the interface yields: u_b^L and u_b^G; X_{1b}^L and X_{1b}^G; ρ_b^L and ρ_b^G; R_d; T_b; and p_b. The interface unknowns are determined from the jump conditions in the conservation of mass density, mass fractions, momentum, and energy; by their very nature, these are computed at the numerical-cell boundary. The interface variables are related by conservation statements to the variables at adjacent nodes located at numerical-cell centers. Viscous effects are neglected because they are generally very small; so are Ma effects. Since the pressure is mainly determined by its far field value, the momentum equation at the interface determines only the very small pressure perturbation.

In mathematical form the conservation statements at $r = R_d$ are:

—mass balance

$$\rho_b^G(u_b^G - dR_d/dt) = \rho_b^L(u_b^L - dR_d/dt). \quad (2.13)$$

We define a mass emission flux, $F_{ems} \equiv -(1/A_d)dM/dt$ that is consistent with $F_{ems} = \rho_b^L(u_b^L - dR_d/dt)$.

—heat balance

$$q_{r,b}^G - q_{r,b}^L = -\{[h_2^G + (h_1^G - h_2^G)X_{1b}^G]/m^G - [h_2^L + (h_1^L - h_2^L)X_{1b}^L]/m^L\}F_{ems} \quad (2.14)$$

where $h_j^G = h_j(p_b, T_b, X_{1b}^G)$, $h_j^L = h_j(p_b, T_b, X_{1b}^L)$ and $h_1^G - h_1^L$ is the heat of evaporation, whereas $h_2^G - h_2^L$ is the heat of solution.

—balance of species 1 flux

$$m_1(J_{1r,b}^G - J_{1r,b}^L) = (Y_{1b}^L - Y_{1b}^G)F_{ems} \quad (2.15)$$

—nonequilibrium evaporation law.

Calculating the fluxes at the molecular level, one obtains

$$F_{ems} = \sum_{j=1,2}[\alpha_{aj}m_j u_{Tj}(n_{j,equil}^G - n_j^G)] \quad (2.16)$$

where $n_{j,equil}^G$s are calculated from thermodynamic relationships [15] and u_{T_j} is the mean molecular velocity crossing a plane in one direction. The expressions for $n_{j,equil}^G$s are

$$n^G_{1,\text{equil}} = [X^L_{1b}\gamma^L_{1b}(\varphi_{1,\text{sat}}/\varphi^G_{1,b})p_{\text{sat},1}(T_b)/(Z^G R_u T_b)]\exp\left(\int_{p_{\text{sat},1}}^{p_b}[v^L_1/(R_u T_b)]\right)dp$$

$$n^G_{2,\text{equil}} = \{\rho^G_b X^L_{2b}\gamma^L_{2b}\exp[(\mu''^L_2 - \mu''^G_2)/(R_u T_b)]\}/(m^G\gamma^G_{2b})$$

where $Z^G = pv(R_u T)$.

To calculate the unknowns from the interface jump relationships we proceed as follows: u^L_b is calculated through the continuity equation in the drop, p_b is given by the far field value and a perturbation calculated from the momentum equation, ρ^L_b and ρ^G_b are calculated from the EOS's once T_b, X^L_{1b} and X^G_{1b} are known, and R_d is calculated from the relationship relating it to F_{ems}. There remains to calculate u^G_b, F_{ems}, X^L_{1b}, X^G_{1b} and T_b. That means that we need to calculate five unknowns from four equations; the degree of arbitrariness in choosing the interface location allows to close the system of equations. In our calculations, X^L_{1b} is specified by the additional use of the species one equation in an inner layer at the drop surface. This choice results in R_d following the regression of the initially pure LO_x; in the spatial region where r is slightly greater R_d, the mass fraction of H_2 is very small.

2.3. Transport properties

2.3.1. Viscosities and thermal conductivities.

Generic plots of viscosities and thermal conductivities vs. T/T_c are very similar [16]. In the low p (ideal gas) regime they exhibit an increase with T, while at high p they exhibit a decrease in the low T regime until a minimum is reached followed by monotonic increase at high T/T_c. In the high $(T/T_c, p/p_c)$ regime, an asymptotic behavior exists for all curves. This variation suggests a protocol for correlating $\eta_i(T,p)$ and $\lambda_i(T,p)$: first we correlate the values in the low p limit as a function of T, then we create an excess function by subtracting the low p function from the high p data, and finally we correlate the high p data vs. (T,p). The oxygen thermal conductivity obtained through this procedure is depicted in Fig. 1 and shows good agreement with the data represented by the circles.

The individual component properties are used with the corresponding states formalism of Teja and Rice [16] to calculate the mixture properties. This procedure uses averaging with weighing factors which are quantities that are functions of critical properties of each component.

To calculate the thermal diffusion factors, we use

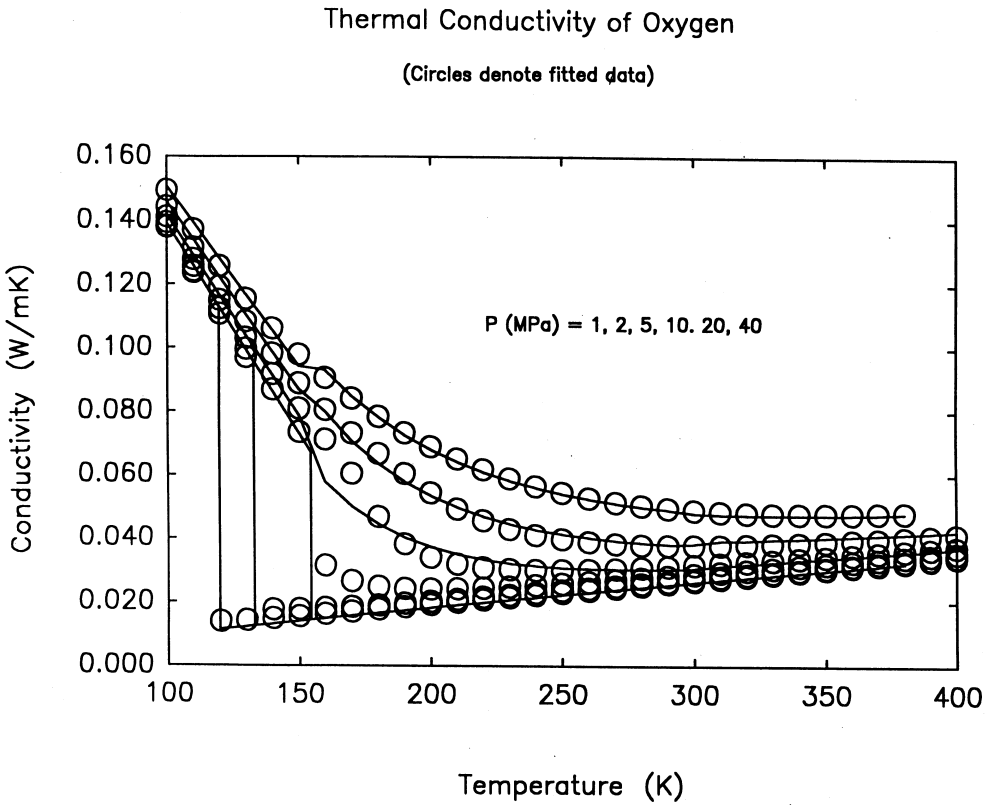

Fig. 1. Fitted values of the oxygen thermal conductivity and comparison with experimental data.

an expression derived for gases and small $(m_i - m_j)$ by Hirshfelder et al. [28]

$$\alpha_T^{(ij)} = \varepsilon_T (m_i - m_j)/(m_i + m_j) \tag{2.17}$$

where ε_T is dependent only on T. According to Bird et al. [29], $\alpha_T^{(ij)}$ is almost independent of concentration for gases. No formalism for calculating $\alpha_T^{(ij)}$ for a general fluid exists to our knowledge. In all results presented here ε_T is taken constant and $\alpha_T = 0.05$. Results from calculations with α_T values of 0.01 and 0.0 at several supercritical pressures are discussed in Harstad and Bellan [23]. Examination of these results shows that they are insensitive to the value of α_T for the compounds considered and in the range of parameters investigated.

2.3.2. Diffusion coefficients

There are four steps in the calculation of the binary diffusion coefficients: first the binary infinite dilution coefficients for a gas are calculated using the formalism of Bird et al. [29]. Second, the infinite dilution coefficients for a liquid are calculated using the formalism of Tyn and Calus [30]. Third, the infinite dilution coefficients for the gas and liquid are combined through an interpolation to yield the infinite dilution coefficients for a binary mixture in both subcritical and supercritical regimes. Fourth, the corresponding states formalism of Teja and Rice [16] is used to calculate the binary diffusion coefficients from the binary infinite dilution coefficients. An example of the calculation appears in Fig. 2.

3. Numerical method

As mentioned above, $Ma \ll 1$, and thus the pressure is calculated as $p(r,t) = p_\infty(t) + p'(r,t)$ where $p_\infty(t)$ is specified and $p'(r,t)$ is a small perturbation calculated from the momentum equation.

The equations are recast in a convenient form for numerical analysis as follows: the density derivatives in equation (2.1) are replaced using the relationship

$$\mathrm{d}\ln\rho = -\alpha_v\,\mathrm{d}T + \kappa_T\,\mathrm{d}p + \sum_1^N (m_j/m - v_j/v)\,\mathrm{d}X_j \tag{3.1}$$

where $\kappa_T = -(1/v)(\partial v/\partial p)_{T,X_j}$ is the isothermal compressibility. Combining equations (3.1), (2.1), (2.10) and (2.11) yields

$$\nabla\cdot\mathbf{u} = -\frac{D\ln\rho}{Dt} = v_\rho - \kappa_s\left(\frac{\mathrm{d}p_\infty}{\mathrm{d}t} + \frac{Dp'}{Dt}\right) \tag{3.2}$$

where the dissipative expansion

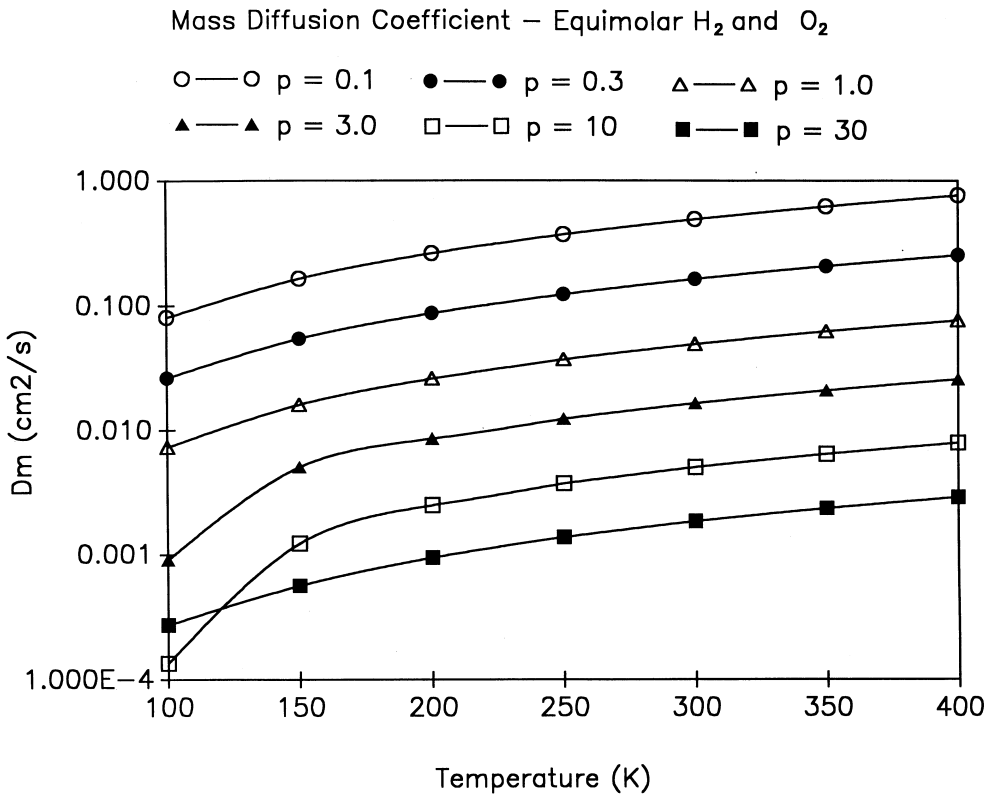

Fig. 2. Calculation of the mass diffusion coefficient for an equimolar mixture of hydrogen and oxygen.

$$v_\rho = \frac{\alpha_v}{nC_p}(\Phi_v - \nabla\cdot\mathbf{q}) + \sum_1^N \left(\frac{\alpha_v}{nC_p}h_j - v_j\right)\nabla\cdot\mathbf{J}_j \qquad (3.3)$$

represents the effect of entropy production and $\kappa_s = \kappa_T - (\alpha_v)^2 T/(nC_p)$ is the isentropic compressibility.

The primitive variables are p, T, X_j (or Y_j), and u_β. The quantities ρ, α_D, C_p, α_v, κ_s, v_j and h_j are calculated from the state equation. At any time step, the solution is found by iterating in two sequential pairs. The first pair is u_r and p'; the second pair is T and Y_1. Spherical symmetry is assumed and the r coordinate is given by a time dependent grid. The thermodynamic variables are calculated at grid cell centers, whereas the velocity and fluxes are calculated at grid cell boundaries. The grid motion is determined by fixing one boundary at the moving interface, $R_d(t)$, and by choosing the outermost boundary, $R_{si}(t)$, to follow the fluid motion (Lagrangian far field boundary); $dR_{si}/dt = u_r(r = R_{si})$. Due to expected sharp gradients, the grid spacing is smallest near the interface.

An iterate of the flow dynamics (u_r, p') pair is done in two steps. First, equation (3.2) is used to produce a predicted velocity when p' is neglected and the small viscous dissipation is estimated by the prior iterate; the interface velocity jump is applied. Second, equations (2.2) and (3.2) are used to correct the velocity and find p' through the use of a potential function.

The second pair of variables, (T, Y_1) is obtained by iteratively solving equations (2.10) and (2.11) as a pair of coupled convection–diffusion equations. Upwind differencing of the convection terms is used in regions of large gradients; relative to the local grid motion, the effective convection velocity is $u_r - dr_g/dt$. The difference equations for the time dependent vectors of cell center values of T and Y_1 are in the form of coupled matrix equations. The matrix elements related to cells at the interface are modified to satisfy the conditions at the interface. At the drop center, the gradients are null; at the far field boundary, the values of the variables are known. During any particular time step, an iterate is accomplished by a two stage process: first, there is a partial explicit time step which is followed by an implicit time step. The implicit time step requires a matrix iteration based on the Thomas algorithm for inverting tridiagonal matrices [31].

Because the time constant associated with equation (2.16) is very small, the equations are very stiff. Therefore, during a time step iterate, a separate iteration is required to calculate the interface conditions. These conditions are then used in the radial velocity calculations and in the formation of the (T, Y_1) vector pair matrices.

4. Results

In order to better understand the trends predicted by this model, we first analyze a baseline calculation and then present a parametric study. During all of our calculations, we monitor the number of phases at each time step and at all locations, for the conditions of this study, only one phase could be found at all times and locations presumably due to the high pressures used here and the peculiarity of the LO_x–H_2 mixture critical locus. Thus, equation (2.16) happens to play no role, although included a priori in the calculations. Therefore, the traditional concept of drop lifetime is meaningless, and the results are presented in terms of variation of the dependent variables over the entire spatial domain without reference to any interface.

4.1. Baseline behavior

The initial conditions for the calculation are: $R_d^0 = 50\times10^{-4}$ cm, $R_{si}^0 = 0.1$ cm, $T_{d,b}^0 = 100$ K (the fluid drop temperature is assumed initially uniform), $T_{si}^0 = 1000$ K, $p = 20$ MPa. The value of R_{si}^0 is large enough so that the fluid drop results are essentially independent of its value. The fluid drop is composed of pure LO_x ($T_c = 154.6$ K, $p_c = 5.043$ MPa), while the surrounding is H_2 ($T_c = 33.2$ K, $p_c = 1.313$ MPa); in order to avoid an initial discontinuity that violates jump conditions, a small amount of oxygen exists initially in the drop surroundings, its distribution vanishing with increasing r.

Figure 3 illustrates the spatial variation of T, ρ and Y_1 ($i = 1$ refers to LO_x) as a function of time. Comparisons between the variation of these quantities show that the density gradient is the steepest, however it does not remain steep during the entire time necessary for drop heating. It is this density gradient that is captured in optical measurements such as Gökalp's [19]; since the gradient eventually relaxes, the optical measurement yields increasingly uncertain results as t increases. The density gradient does not correspond to the Y_1 gradient indicating that it is not the evolution of the pure LO_x fluid drop that is followed in the measurements, but that of an entity into which hydrogen has diffused. The pure LO_x fluid drop shrinks very fast and eventually disappears as shown in Fig. 3 by $Y_1(r = 0) < 1$. It is important to realize that not only do gradients of Y_1 and T occur at different locations, but also that early-time gradients of T are steeper than gradients of Y_1 whereas at later time the opposite is true. In fact, relaxation of the T and ρ profiles occurs much faster than that of Y_1 as seen in the very long time behavior illustrated in Fig. 4. This is because D_T is considerably larger than D_m as shown by their ratio, the traditional Le plotted in Fig. 5. However, while under subcritical conditions Le is the ratio of heat to mass fluxes, under supercritical conditions Le is a misleading measure of the flux ratio [23]. On Fig. 5, an effective Lewis number, Le_{eff}, based upon a boundary layer, quasi-steady estimate of the thermal and mass diffusion length scales [23] is illustrated as well. Com-

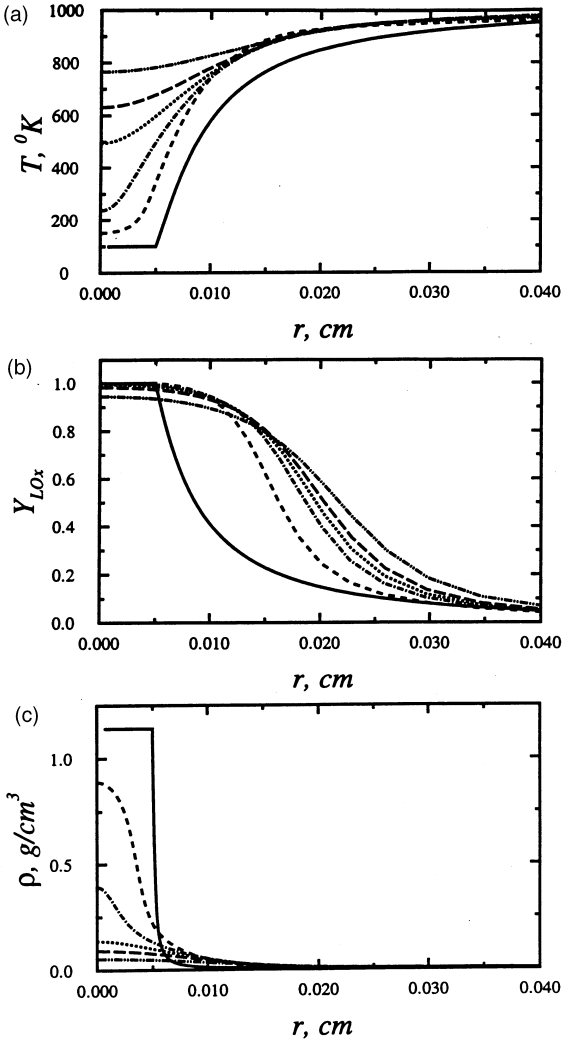

Fig. 3. Spatial variation of the temperature, oxygen mass fraction and density at various times for $R_d^0 = 50 \times 10^{-4}$ cm, $R_{si}^0 = 0.1$ cm, $T_{d,b}^0 = 100$ K, $T_{si}^0 = 1000$ K, and $p = 20$ MPa. The curves correspond to the following times: 0.0 s (—); 7.5×10^{-3} s (- - -); 1.25×10^{-2} s (- · - · -); 1.5×10^{-2} s (· · ·); 1.75×10^{-2} s (– –); 2.414×10^{-2} s (- · · -).

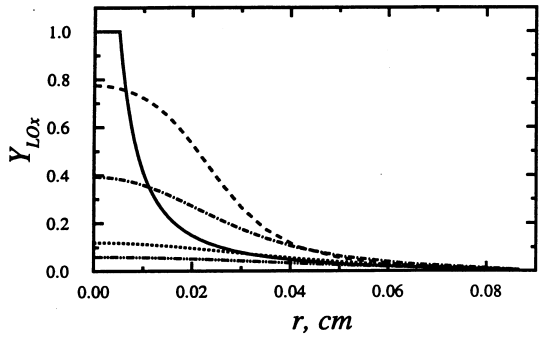

Fig. 4. Long time behavior of the oxygen mass fraction for the initial conditions in the Fig. 3 caption. The curves correspond to the following times: 0.0 s (—); 5×10^{-2} s (- - -); 1×10^{-1} s (- · - · -); 1.5×10^{-1} s (· · ·); 1.763×10^{-1} s (- · · -).

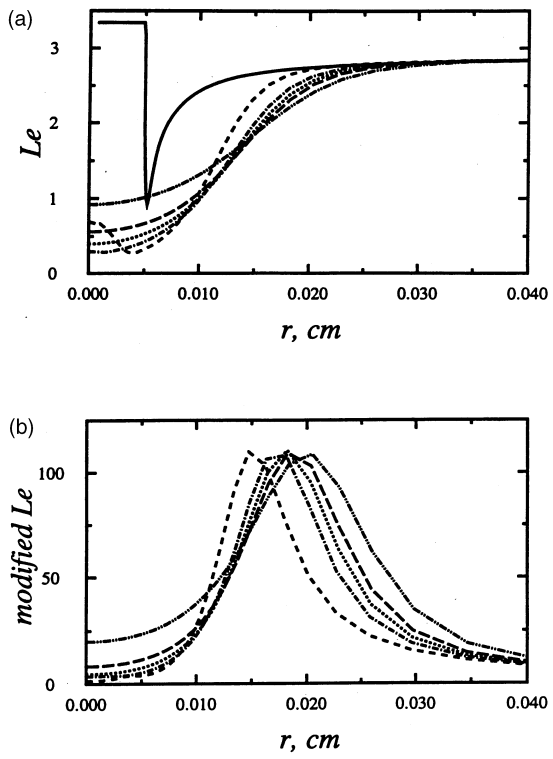

Fig. 5. Spatial variation of the traditional and an effective Lewis number at different times. The initial conditions are those of Fig. 3 caption.

parison of Le vs. Le_{eff} shows that the effective Lewis number is about a factor of 40 larger than the traditional Le. The traditional Le is calculated under the assumption that the molar flux is proportional to mass fraction gradients and the heat flux is proportional to temperature gradients, an assumption that is not satisfied in the present situation. Comparisons between our results and those of Yang et al. [10] for Le shows that we predict similar Le variations, although our values are larger for a given pressure, as will be discussed in the parametric variations below.

Properties related to heat transfer are depicted in Fig. 6: C_p is larger in the fluid drop whereas λ is larger in the drop surroundings. This means that it is more difficult to heat the drop than the drop surroundings (C_p is larger in the drop), and that heat is more difficult to transmit inside the drop than in its surroundings (λ is larger in the drop surroundings than in the drop). Our plots for λ

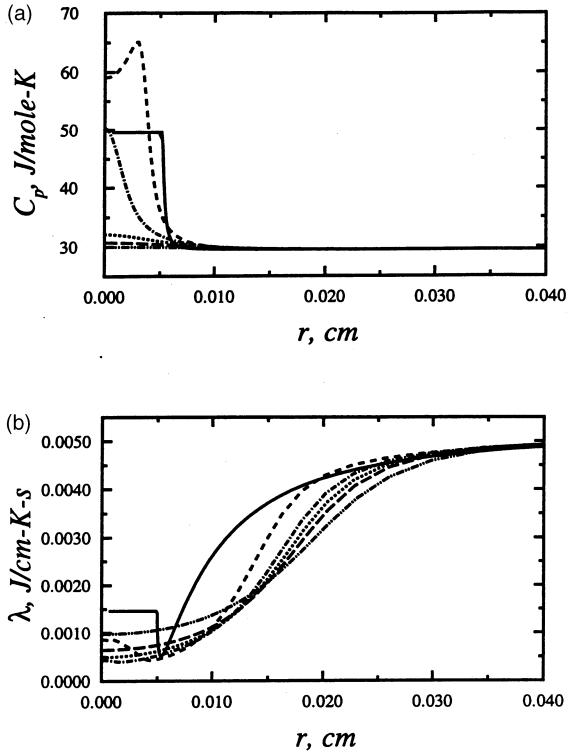

Fig. 6. Spatial variation of C_p and λ for the initial conditions in Fig. 3 caption. Curves are labeled as in Fig. 3 caption.

show a wider scale variation than those of Yang et al. [10] for same R_d^0 and T_{si}^0 but larger p at similar times. As will be seen below, the scales become smaller (i.e. gradients become larger) with increasing pressure and thus our results quantitatively disagree with the small scales shown by Yang et al. [10] at approximately 12.5 MPa (a pressure smaller than that of 20 MPa as in our calculations). It is speculated that the discrepancy comes from our inclusion of additional terms [23] in the model and calculations.

Y_1 vs. T is displayed in Fig. 7 as a function of time in order to parallel previous plots by other authors [17] for very similar supercritical conditions; the only differences are their initial radius of 100×10^{-4} cm and $p = 8$ MPa. Our results show none of the discontinuities displayed by the results of Haldenwang et al. [17] which appeared as a consequence of their equilibrium assumption. The plots in Fig. 7 resemble in shape those of Delplanque and Sirignano [14] obtained also at supercritical conditions ($p = 10.086$ MPa, $T_\infty = 1500$ K) for a burning droplet of identical initial size, although their plots are restricted to a droplet interior whose definition is not given (the criterion for the interface location under supercritical conditions is missing). The small deviation among all curves on Fig. 7 for such a wide time interval suggests almost a similarity solution; this is an unexpected result

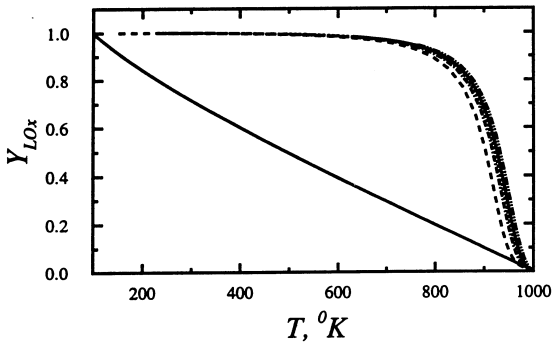

Fig. 7. Temporal variation of the oxygen mass fraction vs. the temperature for the initial conditions in Fig. 3 caption. The curves are labeled as in Fig. 3 caption.

given the complexity of the equations. ρ vs. T is plotted in Fig. 8 as a function of t; away from the initial condition all the plots fall on the same line pointing again to a similarity solution. These plots are for a larger temperature than those of Yang et al. [10] but for a similar pressure regime. Comparisons with those plots are not possible since those results were obtained from phase equilibrium calculations for a liquid mixture of LO_x and H_2.

To evaluate the assumption of constant ρD_m made by other authors [14], we show in Fig. 9 spatial plots of this quantity at different times. The plots show that the initially uniform profiles in each side of the interface evolve strong nonuniformities with time; thus the assumption of constant ρD_m should be discarded from all supercritical regime studies.

4.2. Parametric study

The variation of the above results with initial fluid-drop size, surrounding pressure and surrounding temperature is important for coaxial atomizer design. To

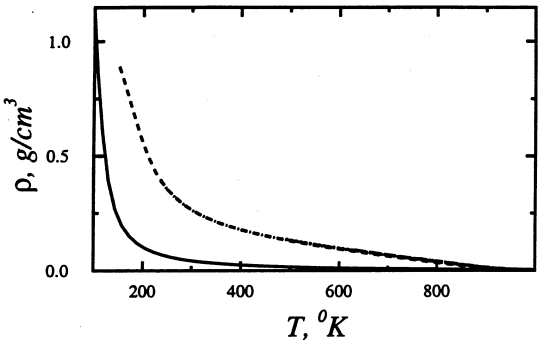

Fig. 8. Temporal variation of the density vs. the temperature for the initial conditions in Fig. 3 caption. The curves are labeled as in Fig. 3 caption.

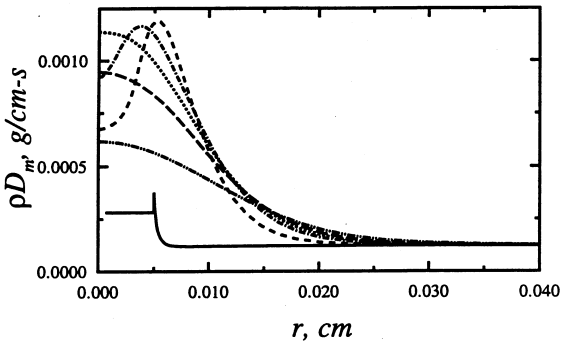

Fig. 9. Spatial variation of ρD_m for the initial condition in Fig. 3 caption. The curves are labeled as in Fig. 3 caption.

explore the impact of these variations, the results of the parametric study are discussed below.

4.2.1. Influence of initial fluid-drop size

To examine the impact of the initial size, calculations were performed with drops of initial radius 25×10^{-4} cm and 300×10^{-4} cm and compared to those of the baseline case; plots of the results at 5×10^{-3} s appear in Fig. 10. The main result of increasing the drop size is to delay drop heating, produce a more uniform LO_x distribution at this time, and maintain the strong density gradient for longer times. Since optical measurements of the interface location correspond to the density gradient, it is expected that experimental information on the interface motion will be more accurate for larger drops.

4.2.2. Influence of surrounding pressure

In Figs 11 and 12 we display results for fixed initial drop size and surrounding temperature as a function of surrounding pressure at 2×10^{-2} s. The slightly larger λ but much larger C_p with increasing p on the LO_x side of the interface (not shown) result in smaller T on the LO_x side of the interface; the opposite occurs on the H_2 side of the interface. Thus, T gradients are greater with increasing p. Increasing the surrounding p decreases both D_m and D_T (not shown); however, there is relatively a larger reduction on the H_2 side of the interface. The decrease in D_m explains the smaller Y_1 on the H_2 side of the interface and the steeper gradients with increasing p. Examination of the ρ profiles shows the considerably larger gradients with increasing p; it is thus inferred that experiments quantifying the interface motion will be more accurate when performed at large pressures. Figure 12 illustrates the spatial variation of ρD_m at different p and confirms that the assumption of constant ρD_m deteriorates with increasing p. This is an expected result since the classical evaluation of D_m as a function of T that is the basis of this assumption is strictly valid only in the limit of the low p (gas) regime.

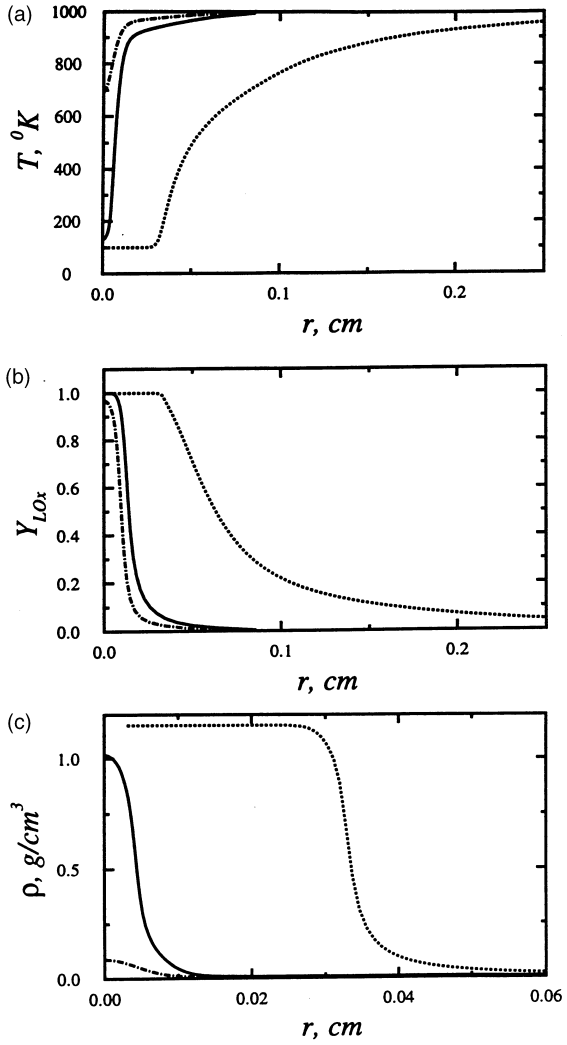

Fig. 10. Spatial variation of the temperature, oxgyen mass fraction and density at 25 MPa. Plots are at 5×10^{-3} s for initial fluid drop radii 25×10^{-4} cm (-·-·-), 50×10^{-4} cm (—) and 300×10^{-4} cm (···).

Examination of the variation of Le with increasing p [23] shows that as p increases, Le remains <1 on the LO_x side of the interface, and decreases with increasing p, whereas Le remains >1 on the H_2 side of the interface and increases with increasing p [23]. This spatial variation with increasing p shows that indeed the gradients become steeper with increasing p. The Lewis number seems insensitive to the pressure in the far field.

The general variation of the dependent variables with increasing p indicates that since the gradients become larger due to a reduction in scales, high pressure combustion in practical devices will have to rely on strong turbulence to enhance mixing and heat transfer.

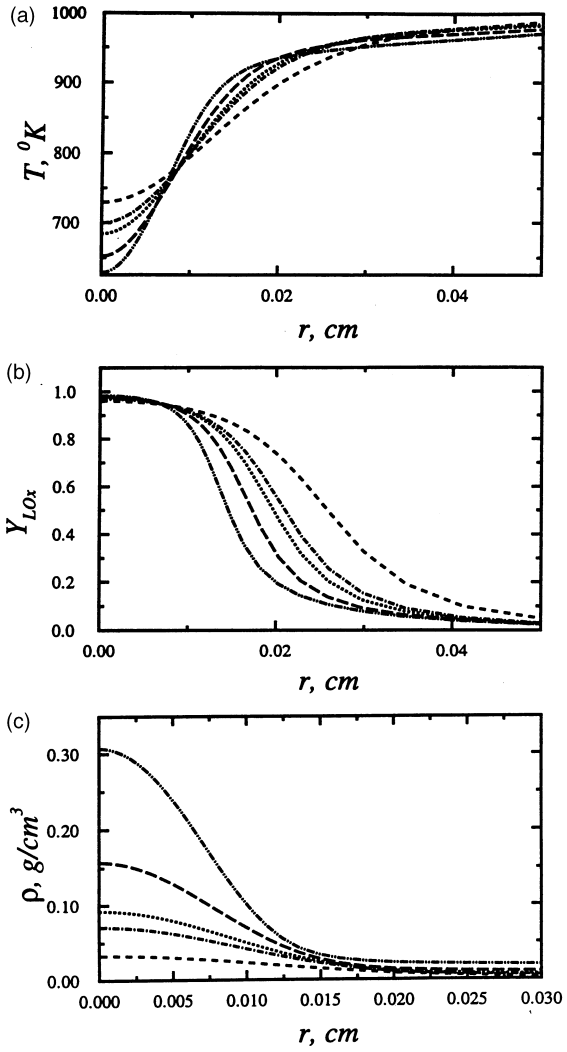

Fig. 11. Spatial variation of the temperature, oxygen mass fraction and density at 2×10^{-2} s for several pressures: 10 MPa (---); 20 MPa (-·--·-); 25 MPa (···); 40 MPa (––); 80 MPa (-···-). Other initial conditions are: $R_d^0 = 50\times10^{-4}$ cm; $R_{si}^0 = 0.1$ cm; $T_{d,b}^0 = 100$ K; $T_{si}^0 = 1000$ K.

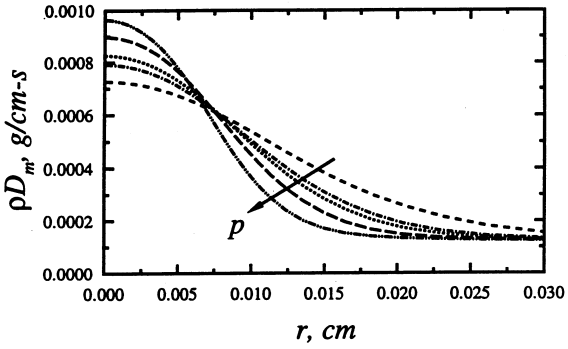

Fig. 12. Spatial variation of ρD_m for the initial condition in Fig. 11 caption. The curves are labeled as in Fig. 11 caption.

4.2.3. Influence of surrounding temperature

Figure 13 contains plots illustrating results at 2×10^{-2} s from calculations at $T_{si}^0 = 1000$ K and 500 K for $p = 20$, 40 and 80 MPa. Spatial plots of the transport properties (not illustrated) show that D_m, D_T and λ all increase with increasing T_{si}^0, however, Le decreases with increasing T_{si}^0 on the H_2 side immediately adjacent to the interface before the asymptotic increasing trend reappears [23]. On the LO_x side of the interface, Le remains <1 and increases with increasing T_{si}^0, however, the difference becomes smaller with increasing p [23]; on the H_2 side of the interface Le remains >1 [23]. This means that scales become smaller with decreasing T_{si}^0, an effect immediately apparent upon examination of the ρ profiles. The larger gradients at smaller T_{si}^0 imply that experiments with drops at lower T_{si}^0 will yield data carrying less uncertainty about the interface motion since it would be more easily detectable.

As expected from the variation of D_m, diffusion of LO_x is enhanced at larger temperatures but the difference decreases with increasing pressure, a result easily observable in Fig. 13. The T plots depicted in Fig. 13 show the same trends regarding the relative gradients magnitude as those found in the plots of ρ and Y_1. The larger T on the LO_x side of the interface with decreasing pressure at the larger T_{si}^0, and the smaller T with decreasing pressure at the smaller T_{si}^0 are the effect of the larger reduction of LO_x at those locations at the larger T_{si}^0; in fact the variation at smaller T_{si}^0 is a snapshot of the early behavior of the drop at larger T_{si}^0.

5. Conclusions

A model of an isolated fluid drop in quiescent, finite spatial surroundings has been derived using the formalism of fluctuation theory. The model presented here is derived from first principles and incorporates all physical aspects of high pressure behavior including Soret and Dufour effects, high pressure mixture-thermodynamics and mixture transport properties over a wide range of pressures and temperatures.

Results obtained for the LO_x–H_2 system show that the supercritical behavior is that of a slow diffusion process. The spatial temperature profile is the first to relax, followed by the density profile; the mass fractions remain nonuniform long after relaxation of both temperature and density. Given the long characteristic time associated with diffusion, it is not surprising that strong turbulence is needed to mix LO_x and H_2 in liquid rocket motors. The

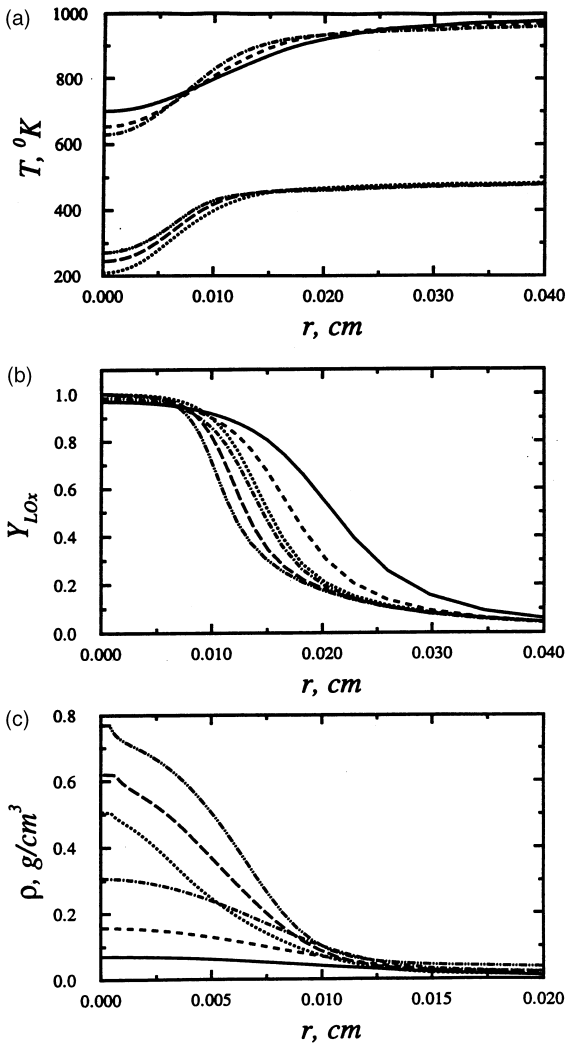

Fig. 13. Spatial variation of the temperature, oxygen mass fraction and density at $T^0_{si} = 1000$ K (—), (- - -) and (- · - · -); and at $T^0_{si} = 500$ K (· · ·), (– –) and (- · · -). The other initial conditions are: $R^0_d = 50 \times 10^{-4}$ cm, $R^0_{si} = 0.1$ cm, and $T^0_{d,b} = 100$ K. Results are at 2×10^{-2} s and for several pressures: 20 MPa (—) and (· · ·); 40 MPa (- - -) and (– –); and 80 MPa (- · - · -) and (- · · -).

results are insensitive to the variation of the thermal diffusion factor (within the range 0.0–0.05 and up to 80 MPa) when this factor is assumed constant with time and uniform [23]. This is remarkable considering that the thermal diffusion factor is the only free parameter in the present calculations. Also unexpected is the self-similar behavior of the LO_x mass fraction vs. the temperature obtained by eliminating the radial variation between the two dependent variables.

An important, although not unexpected finding is that the uniformity assumption for the product of the density by the mass diffusivity is not justified. Additionally, consistent with the different relaxation times of the temperature and mass fractions, the traditional Lewis number is shown to be much smaller than an effective Lewis number estimated from a quasi-steady, boundary layer theory presented elsewhere [23].

Parametric studies performed by varying the initial fluid-drop size, the surrounding pressure and the surrounding temperature show that gradients become larger with increasing pressure and smaller temperatures. The practical consequence of this finding is that increasing turbulence is necessary to mix the reactants at larger pressures.

The above results could not be experimentally validated due to lack of observation of free fluid drops in supercritical, quiescent surroundings. Our results show that optical experimental data must be interpreted with caution since the detected density gradients are maintained only for limited times. In that respect, the most accurate data is expected for large drops in high pressure and low temperature surroundings because the density gradients survive longer with increasing fluid-drop size and pressure, and with decreasing temperature.

Acknowledgements

This research was conducted at the Jet Propulsion Laboratory under sponsorship from the National Aeronautics and Space Administration, the George C. Marshall Space Flight Center with Mr Klaus W. Gross as technical contract monitor. His continuing interest and support are greatly appreciated.

References

[1] Harrje DT, Reardon FH. Liquid Propellant Rocket Combustion Instability. NASA SP-194, 1972.
[2] Williams FA. Combustion Theory. Addison-Wesley, 1965.
[3] Chervinsky A. Transient burning of spherical symmetric fuel droplets. Isr J Technol 1969;7:66–73.
[4] Nuruzzaman ASM, Beer JM. On the nonsteady nature of droplet combustion. Combust Sci and Tech 1971;3:17–24.
[5] Matlosz RL, Leipziger S, Torda TP. Investigation of a liquid drop evaporation in a high temperature and high pressure environment. Int J Heat Mass Transfer 1972;15:831–52.
[6] Rosner DE, Chang WS. Transient evaporation and combustion of a fuel droplet near its critical temperature. Combust Sci and Tech 1973;7:145–58.
[7] Crespo A, Linan A. Unsteady effects in droplet evaporation and combustion. Combust Sci and Tech 1975;11:9–18.
[8] Chesneau X, Chauveau C, Gökalp I. Experiments of high pressure vaporization of liquid oxygen droplets. AIAA 94-0688, 32nd Aerospace Sciences Meeting, Reno, NV, 1994.

[9] Givler SD, Abraham J. Supercritical droplet vaporization and combustion studies. Prog Energy Combust Sci 1996;22:1–28.
[10] Yang V, Lin N, Shuen J-S. Vaporization of liquid oxygen (LOX) droplets in supercritical hydrogen environments. Combust Sci and Tech 1994;97:247–70.
[11] Scheibel EG. Liquid diffusivities. Industrial Engineering Chemistry 1954;46:2007–8.
[12] Takahashi S. Preparation of a generalized chart for diffusion coefficients of gases at high pressures. Journal of Chemical Engineering (Japan) 1974;7:417–20.
[13] Hsiao GC, Yang V, Shuen JS. Supercritical vaporization and dynamics of liquid oxygen (LOX) droplet in hydrogen stream. AIAA 95-0383, 33rd Aerospace Sciences Meeting, Reno, NV, 1995.
[14] Delplanque J-P, Sirignano WA. Numerical study of the transient vaporization of an oxygen droplet at sub- and super-critical conditions. Int J Heat Mass Transfer 1993;36(2):303–14.
[15] Prausnitz J, Lichtenthaler R, de Azevedo E. Molecular Thermodynamics for Fluid-phase Equilibrium. Prentice-Hall, 1986.
[16] Reid RC, Prausnitz JM, Polling BE. The Properties of Gases and Liquids, 4th ed. McGraw-Hill Book Company, 1987.
[17] Haldenwang P, Nicoli C, Daou J. High pressure vaporization of LOX droplet crossing the critical condition. Int J Heat Mass Transfer 1996;39(16):3453–64.
[18] Sato J, Tsue M, Niwa M, Kono M. Effects of natural convection on high-pressure droplet combustion. Combust and Flame 1990;82:142–50.
[19] Chauveau C, Gökalp I. Experiments on the vaporization of LO_x droplets under high pressure, submitted, 1997.
[20] Chauveau C, Chesnau X, Gökalp I. Burning characteristics of *n*-heptane droplets. AIAA 93-0824, 31st Aerospace Sciences Meeting, Reno, NV., 1993.
[21] Chauveau C, Chesnau X, Gökalp I. High pressure vaporization and burning of methanol droplets in reduced gravity. AIAA 94-0430, 32nd Aerospace Sciences Meeting, Reno, NV., 1994.
[22] Harstad KG, Miller RS, Bellan J. Efficient high pressure state equations. AIChE 1997;43(6):1605–10.
[23] Harstad K, Bellan J. The Lewis number under supercritical conditions, submitted, 1997.
[24] Bellan J, Summerfield M. Theoretical examination of assumptions commonly used for the gas phase surrounding a burning droplet. Combust and Flame 1978;33:107–22.
[25] Keizer J. Statistical Thermodynamics of Nonequilibrium Processes. Springer-Verlag, New York, 1987.
[26] Peacock-Lopez E, Woodhouse L. Generalized transport theory and its application to binary mixtures. In : Matteoli E and Mansoori GA (Eds.). Fluctuation Theory of Mixtures, Advances in Thermodynamics. Taylor and Francis, 1983;2:301–33.
[27] Bellan J, Cuffel R. A theory of non-dilute spray evaporation based upon multiple drop interaction. Combust and Flame 1983;51(1):55–67.
[28] Hirshfelder JO, Curtis CF, Bird RB. Molecular Theory of Gases and Liquids. John Wiley and Sons, 1964.
[29] Bird RB, Stewart WE, Lightfoot EN. Transport Phenomena. John Wiley and Sons, 1960.
[30] Tyn MT, Calus WF. Diffusion coefficients in dilute binary mixtures. J of Chem Eng Data 1975;20(1):106–9.
[31] Anderson DA, Tannehill JC, Pletcher RH. Computational Fluid Mechanics and Heat Transfer. Hemisphere, NY, 1984.